

Abstract

We use global coupled atmosphere-ocean-biogeochemistry models from the Coupled Model Intercomparison Project (CMIP5), under the RCP8.5 scenario, to show that the global interannual variability of the sea surface $p\text{CO}_2$ (calculated as 1σ) could increase by $62 \pm 22\%$ by 2090. This amplification is a consequence of a larger background $p\text{CO}_2$ and a lower buffering capacity that enhance the response of $p\text{CO}_2$ to surface temperature (T) and dissolved inorganic carbon (DIC) changes. The amplification is counteracted by a decrease in the sea-surface DIC interannual variability, which will likely cause a strong reduction on the $p\text{CO}_2$'s variability in the equatorial Pacific. The potential changes in seawater carbonate chemistry are simulated with higher consistency than those in the DIC and T anomalies driven by ocean circulation and biology. The changes in sea-surface $p\text{CO}_2$ interannual variability are reflected in the ocean-atmosphere flux of CO_2 and need to be accounted for future carbon projections.

Plain Language Summary

We used models to show that the variations in the ocean surface partial pressure of carbon dioxide, that occur between one and ten years, will be larger by the end of the 21st century in most of the ocean. This is because the human carbon emissions make the ocean less able to buffer the natural changes in the total amount of inorganic carbon and temperature that are driven by physics and biology. The models also show that the fluctuations in the total inorganic carbon will be smaller in the future, reducing the variations of the partial pressure of carbon dioxide in the equatorial Pacific. The changes in the ocean's carbon are reflected in the flux of carbon between the atmosphere and the ocean.

1 Introduction

On average, the ocean absorbs 2.4 ± 0.5 Pg of carbon each year (Le Quéré et al., 2018) but this amount varies on interannual time-scales. Efforts have been made to estimate the interannual variability of CO_2 uptake in observations and models (Dong et al., 2017), however there is little agreement with values ranging from ± 0.14 PgC yr⁻¹ for 1982-2007 (Park et al., 2010), ± 0.29 1985-2017 (Le Quéré et al., 2018) to ± 0.40 PgC yr⁻¹ for 1997-97 (Le Quéré et al., 2000). The CO_2 ocean-atmosphere flux is determined by the difference between ocean and atmospheric $p\text{CO}_2$, and it is further modulated by wind speed variations and sea ice coverage. As the atmospheric $p\text{CO}_2$ is largely uniform around the globe, most of the interannual variability is controlled by the sea surface $p\text{CO}_2$ which is determined by surface dissolved inorganic carbon (DIC), total alkalinity (TA), temperature (T) and salinity (S). Large scale atmosphere-ocean interactions, such as the El Niño Southern Oscillation (ENSO) in the equatorial Pacific, the Pacific Decadal Oscillation (PDO) in the North Pacific, the Southern Annular Mode (SAM) in the Southern Ocean, and the North Atlantic Oscillation (NAO) (McKinley et al., 2004; Friedrich et al., 2006; Landschützer et al., 2019) induce changes in physical circulation and biology that alter DIC, TA, T and S ultimately impacting the CO_2 flux. The effect of DIC, TA, T and S interannual anomalies on the $p\text{CO}_2$ depends on how sensitive the water carbonate chemistry is to these changes. In the ocean, approximately 89% of the dissolved inorganic carbon is in the form of bicarbonate (HCO_3^-) and $\approx 10.5\%$ as carbonate (CO_3^{2-}); the CO_2 concentration ($[\text{CO}_2]$) only comprises a $\approx 0.5\%$ (Zeebe & Wolf-Gladrow, 2001). As the ocean captures CO_2 , its ability to convert it into HCO_3^- and CO_3^{2-} decreases, and the $p\text{CO}_2$ sensitivity to any change in DIC increases. In the same way, a larger background $[\text{CO}_2]$ enhances the effect of temperature on $p\text{CO}_2$'s solubility. Recently, it was shown that the sea-surface $p\text{CO}_2$ is already experiencing a seasonal amplification (Landschützer et al., 2018; Gorgues et al., 2010) which is projected to increase further according to model projections (Gallego et al., 2018; Fassbender et al., 2017; McNeil & Sasse, 2016; Hauck

66 & Völker, 2015). Yet the question remains unresolved whether the amplification will also
 67 occur for other time-scales. Interannual changes in ocean surface pCO₂ may affect the
 68 oceanic sink of anthropogenic CO₂; for example in 2013 the North Pacific subtropical
 69 gyre was a net annual source of CO₂ for the first time, due high pCO₂ caused by warm
 70 anomalies (Sutton et al., 2017), and during the 2015-2016 El Niño the CO₂ outgassing
 71 in the equatorial Pacific was reduced by 26 to 54% (Chatterjee et al., 2017). The cur-
 72 rent observational time series are not long enough to detect changes in interannual to
 73 multi-decadal scales, therefore we rely on Earth System Models (ESMs) to project fu-
 74 ture changes. Our aim is to quantify how well the CMIP5 models represent the mech-
 75 anisms of present-day sea surface pCO₂ interannual variability (from now referred as IAV)
 76 when compared to data-based estimates, and from there, elucidate the future interan-
 77 nual variability amplification (IAVA) of the carbon cycle in response to greenhouse gases
 78 and global warming and the possible consequences for the ocean-atmosphere flux of CO₂.

79 2 Methodology

80 Models

81 For our analysis, sea surface FCO₂, pCO₂, DIC, TA, T and S monthly-mean out-
 82 put variables covering the period from 1861-2005 were obtained from historical simula-
 83 tions, and the period 2006-2100 from future climate change simulations under the Rep-
 84 resentative Concentration Pathway 8.5 (RCP8.5) (IPCC, 2013). We selected 15 fully cou-
 85 pled earth system models that participated in the Coupled Model Intercomparison Project,
 86 Phase 5 (CMIP5) to analyze the standard deviation of pCO₂. Out of the fifteen, we se-
 87 lected six models for a more comprehensive analysis of the causes driving pCO₂ variabil-
 88 ity; these models were selected based on data availability: CanESM2, CESM1-BGC, GFDL-
 89 ESM2M, MPI-ESM-LR, HadGEM2-ES and HadGEM2-CC (See supplementary materi-
 90 al of Hauri et al. (2015)). The ocean’s surface data sets were regridded onto a 1°x1° grid
 91 using Climate Data Operators (CDO). The Arctic Ocean and the region poleward of 70°S
 92 are removed from the analyses, because observational data for model validation are scarce.

93 Analysis

94 Commonly, the interannual anomalies are defined as deviations of monthly output
 95 values from a mean climatology, or by using a running 12 month filter on detrended monthly
 96 values. However, for CMIP5 models, the future seasonal cycle of pCO₂ is expected to
 97 increase (Gallego et al., 2018), therefore removing a mean climatology for the 1861-2100
 98 period would result in an overestimation of IAVA. On the other hand, a 12 month run-
 99 ning filter would remove important sub-annual information and removing a linear trend
 100 from a 200-year-long time series poses its own difficulties. To avoid these issues, we cal-
 101 culate the monthly anomalies for each year as the monthly deviation from a 11-year run-
 102 ning climatology centered on that year. For example, for the year 1935 we desasonalize
 103 the monthly values by subtracting the mean climatology from 1930 to 1940; for the year
 104 1936 we use the climatology from 1931-1941 and so on. (Supplement Figure S1 shows
 105 the running climatology for pCO₂ and the anomalies obtained with this method). To
 106 elucidate the underlying physical and chemical processes controlling the pCO₂ interan-
 107 nual anomalies (from now pCO₂’) we calculated a first order Taylor series expansion of
 108 pCO₂’ in terms of its four controlling factors, DIC, TA, T and S. To remove the fresh wa-
 109 ter concentration/dilution effect we use salinity-normalized DIC and TA using a mean
 110 salinity of 35 psu, referred as DIC_s and TA_s, (Lovenduski et al., 2007). The freshwater
 111 effect is now included in the S_{fw} term. For the Taylor series expansion, each variable (X
 112 = DIC_s, TA_s, T and S_{fw}) is decomposed as $X = \bar{X} + X'$. The term \bar{X} represents the
 113 running climatology and X' denotes the interannual anomaly. The full first-order series
 114 expansion is given by:

$$pCO_2' \approx \frac{\partial pCO_2}{\partial DIC} \Big|_{\frac{TA, DIC}{T, S}} DIC_s' + \frac{\partial pCO_2}{\partial TA} \Big|_{\frac{TA, DIC}{T, S}} TA_s' + \frac{\partial pCO_2}{\partial T} \Big|_{\frac{TA, DIC}{T, S}} T' + \frac{\partial pCO_2}{\partial S} \Big|_{\frac{TA, DIC}{T, S}} S_{fw}' \quad (1)$$

115

116 where the derivatives are evaluated on the running climatologies. The full deriva-
 117 tion of Eq. (1) is given in the Supplementary material. Equation (1) can be rewritten
 118 as:

$$pCO_2' \approx \overline{pCO_2} \cdot (\gamma_{DIC_s} \cdot DIC_s' + \gamma_{TA_s} \cdot TA_s' + \gamma_T \cdot T' + \gamma_S \cdot S_{fw}') \quad (2)$$

119

120 Where, for notation purposes, each derivative is re-defined as: $\gamma_X = \frac{1}{\overline{pCO_2}} \cdot \frac{\partial pCO_2}{\partial X}$,
 121 and we will refer to them as the *pCO₂ sensitivity to X*. To determine how much each term
 122 contributes to the variability of pCO₂' Equation (2) is multiplied by pCO₂', and then av-
 123 eraged, obtaining the following equation:

$$\begin{aligned} \langle (pCO_2')^2 \rangle &\approx \overline{pCO_2} \cdot \gamma_{DIC_s} \langle DIC_s' \cdot pCO_2' \rangle + \overline{pCO_2} \cdot \gamma_{TA_s} \langle TA_s' \cdot pCO_2' \rangle + (3) \\ &\quad \overline{pCO_2} \cdot \gamma_T \langle T' \cdot pCO_2' \rangle + \overline{pCO_2} \cdot \gamma_S \langle S_{fw}' \cdot pCO_2' \rangle, \end{aligned}$$

124

125 where $\langle \dots \rangle$ represents a temporal averaging operator. Introducing the follow-
 126 ing notation:

$$\beta_X \equiv \frac{\langle \overline{pCO_2} \cdot \gamma_X \cdot X' pCO_2' \rangle}{\langle (pCO_2')^2 \rangle} \quad (4)$$

127

, we can then divide Eq. (3) by $\langle (pCO_2')^2 \rangle$ to give the relationship $\sum_X \beta_X = 1$,
 128 where $X = \{DIC, TA, T, S\}$, as introduced by Doney et al. (2009). Thus, if we multiply
 129 Eq.(4) by the root-mean-square (RMS) of the anomalies (defined as $\sqrt{\langle (pCO_2')^2 \rangle}$),
 130 then the β_X coefficients can be interpreted as the fraction of the total pCO₂' RMS that
 131 each variable contributes. In our numerical calculations the sum of the β 's differs slightly
 132 from one due the approximation used for the Taylor expansion, and the anomalies av-
 133 eraged being slightly different from zero.

134

3 Results

135

The increase in IAV of surface pCO₂' is illustrated with the running standard de-
 136 viation of the monthly anomalies from 1871 to 2090 (Figure 1). The ensemble mean of
 137 the globally averaged STD of pCO₂ increases from 6 μ atm to 11 μ atm by the end of the
 138 21st century. Detailed global maps of the 1866-1917 and 2045-2095 STD are found in Sup-
 139 plement material S2 and S3. For the pCO₂, a present day comparison shows that the
 140 1987-2010 models STD is about 7 μ atm and is larger than the observation-based esti-
 141 mates of ≈ 3.2 μ atm (Landschützer et al., 2017) (excluding the Arctic region).

142

Present day sea surface pCO₂ interannual variability

143

To evaluate the models ability to represent the IAV, we compare the root mean square
 144 (RMS) of simulated pCO₂' for the 1987-2010 period with data-based estimates of Landschützer

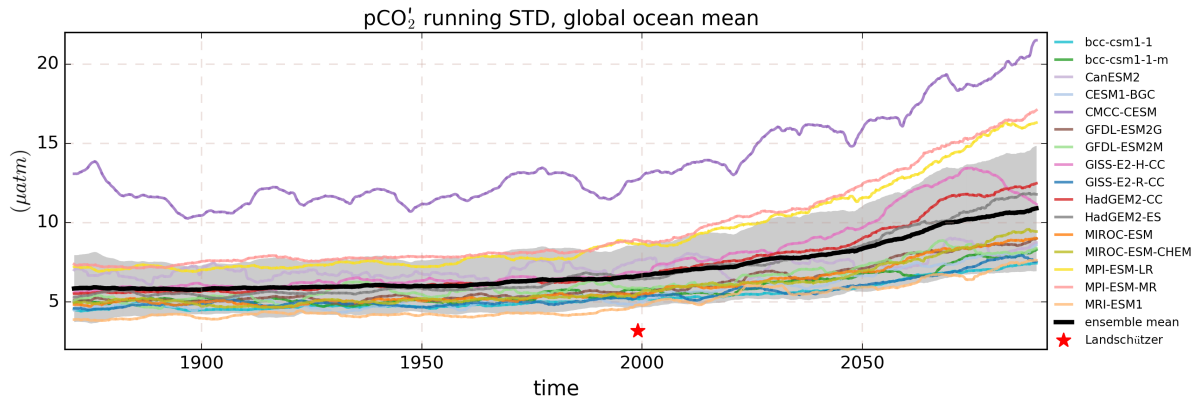


Figure 1. Increase in IAV of the sea surface $p\text{CO}_2'$ as a function of time. The IAV is expressed as the running standard deviation (STD) of the monthly anomalies simulated for the historical and the high-emissions Representative Concentration Pathway 8.5 from 1861 to 2100. The STD is calculated using a 10 years moving window for each grid point and then globally averaged. The monthly anomalies for each year were calculated by removing a 11-year climatology centered around that year, in order to remove the positive trend and the increasing seasonal cycle amplitude. The final STD time series comprises the 1871-2090 period. Solid black line indicates the ensemble mean of the individual STDs; the grey area, $\pm 1\sigma$. The STD of the Landschützer et al. (2017) data set for the period 1987-2010 is indicated by a red star.

145 et al. (2017) (Figure 2, first column). The models CanESM2, CESM1-BGC and GFDL-
 146 ESM2M show the largest $p\text{CO}_2$ variability in the equatorial Pacific in agreement with
 147 the data-based estimates, while for HadGEM2-CC/ES and MPIESM-MR, the strongest
 148 fluctuations occur in the high latitudes, especially in the Southern Ocean and North At-
 149 lantic. Other observation-based estimates by Rödenbeck et al. (2014) show that the equa-
 150 torial belt (15°S to 15°N) accounts for 40% of the total temporal standard deviation of
 151 the global Ocean. The low equatorial variability in the HadGEM2-CC/ES and MPI-ESM-
 152 MR models may be a consequence of the CO_2 flux variability that exhibits a much shorter
 153 period variation than ENSO time-scales, thus ENSO does not play a dominant role and
 154 the high latitudes dominate the variability (Dong et al., 2016).

155 Models exhibit a higher variability in the subtropical gyres and the high latitudes
 156 when compared to the data-based estimate of Landschützer et al. (2017); however the
 157 data-based estimations are an interpolation of the Surface Ocean CO_2 Atlas (SOCAT)
 158 dataset (Bakker et al., 2016; Sabine et al., 2013) which may be biased due to under-sampling,
 159 and interpolation methods may cause a lower RMS in high latitudes with limited obser-
 160 vational coverage (Landschützer et al., 2019). For example, the data-base product of Rödenbeck
 161 et al. (2015), which also uses the SOCAT data, shows lower $p\text{CO}_2$ values than mooring
 162 time series. This is related to the lack of measurements in some areas and seasons or be-
 163 cause moorings are not representative of larger areas (Sutton et al., 2017). In another
 164 study, Tjiputra et al. (2014) found that the 1970-2011 deseasonalized $p\text{CO}_2$ anomalies
 165 of the second release of the SOCAT dataset (Bakker et al., 2014) show a larger standard
 166 deviation than the models, but they were of equal magnitude when the models were sub-
 167 sampled to the measurements' areas. The values reported by Landschützer et al. (2019)
 168 are lower than the Tjiputra et al. (2014) for all regions. Moreover, the local interannual
 169 variability can be much larger when looking at individual time series. For example, Sutton
 170 et al. (2014) found that in the Niño 3.4 central equatorial Pacific index region the $p\text{CO}_2$
 171 annual mean ranged from 315 to 578 μatm between 1997 and 2011.

172 The drivers of the $p\text{CO}_2'$ variability are analyzed in Figure 2 using the decompo-
 173 sition of Eq. (4). Figure 2, columns d, e, f and g show the respective contributions of T,
 174 DIC, TA and S to the RMS of the $p\text{CO}_2'$ for the 1987-2010 period. We compare the re-
 175 sults with the Landschützer et al. (2017) estimates for which we calculate only the ther-
 176 mal and non-thermal components (TA and DIC are not available). The non-thermal com-
 177 ponent comprises the combined contribution of DIC, TA and S, (Takahashi et al., 2002).
 178 The thermal and non-thermal contributions calculated for the CMIP5 models can be found
 179 in Supplement material (Figure S4); these follow the DIC and T patterns. The regional
 180 dominance of the thermal and non-thermal components on the IAV emulates that of its
 181 seasonal cycle; the high latitudes, and the strong upwelling region of equatorial Pacific
 182 are dominated by non-thermal changes; whereas the subtropical gyres are controlled by
 183 the solubility changes induced by temperature variations (Landschützer et al., 2019). In
 184 the equatorial Pacific, HadGEM2-CC/ES and MPIESM-MR show that during El Niño
 185 years the $p\text{CO}_2$ anomalies are positive due to increased temperatures induced by the anoma-
 186 lous eastward advection of warmer waters; while CanESM2, CESM1-BGC and GFDL-
 187 ESM2M suggest that the redistribution of oceanic currents and reduced upwelling of DIC-
 188 rich waters generates negative $p\text{CO}_2$ anomalies (Jin et al., 2019). The DIC-dominated
 189 models are in agreement with results obtained from observations (Feely et al., 2006; Sut-
 190 ton et al., 2014), an offline model driven by reanalysis ocean products (Valsala et al., 2014)
 191 and a hindcast simulation (Doney et al., 2009). The observed $p\text{CO}_2'$ associated with El
 192 Niño are negative and are predominantly caused by wind driven changes in the currents
 193 that alter the DIC distribution, rather than by changes in temperature (Doney et al.,
 194 2009; Valsala et al., 2014; Long et al., 2013; Feely et al., 1999; Cosca et al., 2003). The
 195 models that fail to represent the dominance of DIC on $p\text{CO}_2$ IAV in the equatorial Pa-
 196 cific, present a weak reduction in upwelling during El Niño years and weak vertical gra-
 197 dients of DIC (Jin et al., 2019). In the equatorial Atlantic region only the HadGEM2-
 198 CC/ES shows a temperature dominance (Wang et al., 2015), disagreeing with the Landschützer
 199 et al. (2019) estimate. Only the HadGEM2-CC/ES model shows a relatively important
 200 alkalinity contribution in the North Atlantic and North Pacific that counteracts the pos-
 201 itive DIC contribution. Salinity has a minor effect everywhere, with a small positive ef-
 202 fect in the western Pacific associated with rainfall changes due ENSO. Models agree with
 203 the data estimates on the non-thermal dominance in the high latitudes (Figure 2). The
 204 Southern Ocean $p\text{CO}_2$'s IAV is the result of increased upwelling of DIC-rich waters caused
 205 by stronger winds related to the southern annular mode (Resplandy et al., 2015; Verdy
 206 et al., 2007). In the sub-polar North Atlantic the observations show a non-thermal dom-
 207 inance north of 40°N , while in the models the DIC dominance extends to $25\text{-}30^\circ\text{N}$.

208 *Future sea surface $p\text{CO}_2$ interannual variability*

209 The sea surface $p\text{CO}_2$ IAV, calculated as the RMS-value of the interannual $p\text{CO}_2$
 210 anomalies, is amplified in most of the ocean by the end of the 21st century (Figure 3a),
 211 (see Supplement material Figure S5 for each individual model). Yet, the magnitude of
 212 the IAV amplification (IAVA) exhibits large regional differences, and even decreases in
 213 the equatorial Pacific for some models. Here, we analyze the causes of IAVA and its spa-
 214 tial heterogeneity by separating the analysis into two groups of models according to their
 215 behavior. The first group includes the CanESM2, CESM1-BGC and GFDL-ESM2G. They
 216 exhibit the maximum IAV in the equatorial Pacific, which decreases in the future and
 217 is dominated by DIC (see Figure 3a, upper row). The second group includes the HadGEM2-
 218 CC/ES and MPI-ESM-IR models, and is characterized by maximum IAV in the high lat-
 219 itudes (especially in the Southern Ocean), a temperature dominance in the equatorial
 220 Pacific's IAV and an increase in future IAV everywhere (see Figure 3a, bottom row). The
 221 same behavior is observed in the ocean-atmosphere CO_2 flux (FCO_2) (Figure 3c). The
 222 pattern correlation between the change on RMS of $p\text{CO}_2'$ and the change on RMS of FCO_2'
 223 is in the order of 0.5 to 0.8 depending on the model (not shown). This indicates that in-
 224 creased $p\text{CO}_2$ IAV is one of the main drivers of the FCO_2 IAV increase. However, ad-

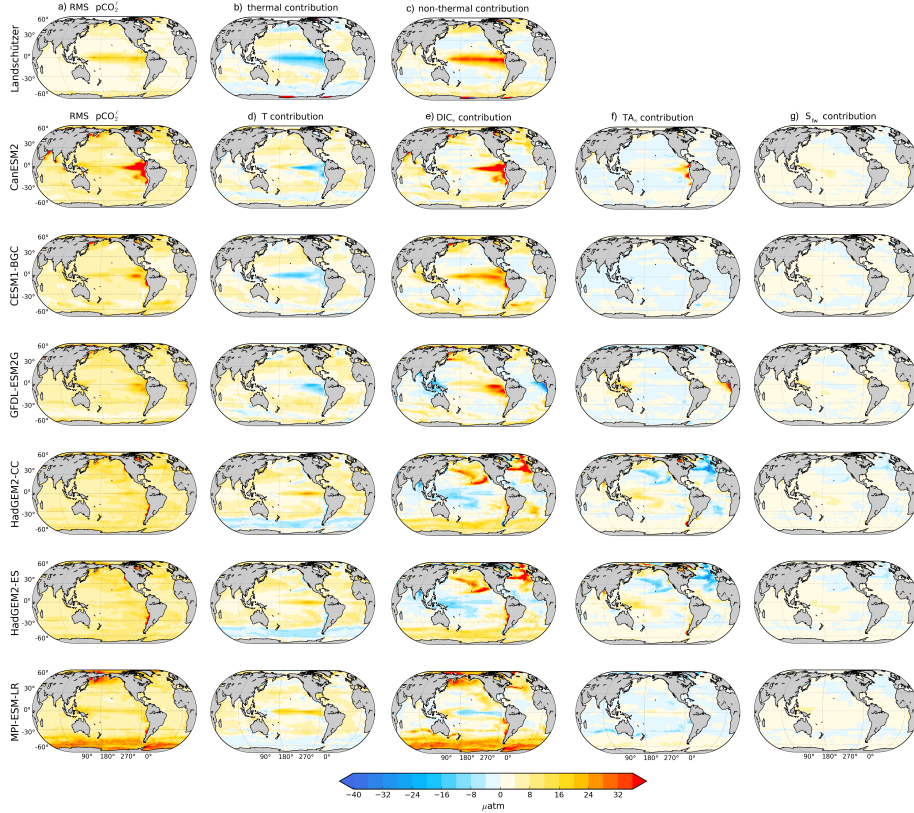


Figure 2. Mechanisms driving the 1987-2010 interannual variability of surface ocean $p\text{CO}_2$. First row shows the **a)** Landschützer et al. (2017) estimate of the root mean square (RMS) of $p\text{CO}_2$ interannual anomalies, and its **b)** thermal and **c)** non-thermal contributions. Panels on the second to seventh rows show the different CMIP5 models **a)** root mean square (RMS) of $p\text{CO}_2$ interannual anomalies and its contributions from **d)** temperature (T), **e)** salinity normalized dissolved inorganic carbon (DIC_s), **f)** salinity normalized total alkalinity (TA_s) and **g)** salinity including fresh water effect (S_{fw}). For the observations, we calculate a thermal and non-thermal terms following Takahashi et al. (2002) method because there is not enough DIC, TA and S data available. The non-thermal component comprises the combined effects of DIC, TA and S. Following the method of Doney et al. (2009), each map of the contributions is calculated as the β coefficient of Eq. (4) normalized by the RMS of the $p\text{CO}_2$. In the panels, yellow-redish colors indicate a positive contribution to the RMS of $p\text{CO}_2$ interannual anomalies and blue colors represent a negative contribution.

ditional substantial contributions coming from changes in wind speed and solubility also play a role.

We now set to determine how much of the $\overline{pCO_2}$ IAVA is due to changes in mean background carbonate chemistry and how much can be explained by changes in physical and biological processes. To this aim, we calculate the RMS of $\overline{pCO_2}'$ for the final period as if only the background carbonate chemistry - represented by $\overline{pCO_2}$ and the sensitivities (γ_T and γ_{DIC})- increase, but maintaining the initial values of the anomalies given by T' and DIC_s' (see Eq. (2)). The later anomalies are the result of physical and biological variations. In both groups of models, the case in which only the carbonate chemistry is changed shows a global mean IAVA 3.4 times larger than for the case in which DIC_s' and T' are also allowed to vary (compare in Figure 3b with 3a). The large increase in $\overline{pCO_2}$ and γ_{DIC} is similar for both groups of models and generate an overall amplification (Figure 4a,b). It is important to mention that the separation between $\overline{pCO_2}$ and γ_{DIC} is a mathematically construct rather than two separate phenomena. Ultimately, the change in $\overline{pCO_2} \cdot \gamma_{DIC}$ is what determines the increase in the DIC contribution, while the T contribution increases almost exclusively due to the increase in $\overline{pCO_2}$ since γ_T remains almost unchanged (not shown).

The damping of the $\overline{pCO_2}$ IAVA in the case where both, carbon chemistry and interannual anomalies change is due to a decrease of the DIC' interannual variability (Figure 4a). The simulations differ in DIC' creating a large spread in the projected IAVA. For example, in the first group of models, the DIC standard deviation has a maximum in the equatorial Pacific and decreases in the future by $\approx 41\%$ causing a decrease in $\overline{pCO_2}$ IAV in the region (Figure 4c). For the MPI-ESM-LR and HadGEM-ES/CC the DIC anomalies are smaller in the equatorial region but increase by $\approx 8\%$, enhancing the IAVA. In high latitudes, the DIC STD decreases for both groups of models, but they present a larger sensitivity and a more rapid increase in $\overline{pCO_2}$ than the mid-low latitudes (Figure 4a,b), which agrees with previous studies (Bates et al., 2014; Egleston et al., 2010). Of the two groups of models, the MPI-ESM-LR and HadGEM-ES/CC show a smaller decrease in DIC' and a larger increase in the sensitivity, and therefore result in a larger $\overline{pCO_2}$ IAVA than the CanESM2, CESM1-BGC and GFDL-ESM2G. Interestingly, the T' anomalies remain of similar magnitude during both periods of time, which makes the overall T contribution to $\overline{pCO_2}$ be more amplified than the DIC contribution (see Supplement material, Figure S6).

The intra-model differences on DIC' and T' IAV arise from the differences in physical and biological controls, or due to changes in the main modes of ocean-atmosphere variability, such as ENSO, NAO, SAM and PDO. An in-depth analysis of these causes is beyond the scope of this paper, but we discuss some possible explanations found in the current literature. One of the reasons for the diminished DIC' variability under future emission scenarios, may be related to the fact that climate models simulate a weaker Walker circulation in response to global warming (Vecchi et al., 2006; Zhao & Allen, 2019); this would weaken the upwelling of DIC-rich waters during La Niña conditions. Other studies suggest a future increase in ENSO amplitude and a weakening of the Walker circulation, will increase the frequency of the eastward propagation of warm waters (Timmermann et al., 1999; Cai et al., 2015, 2018). Moreover, Cai et al. (2018) found that models that accurately represent the ENSO features, also show a future increase in ENSO's frequency; this indicates that the reduction of DIC variability cannot be controlled solely by changes in the climate modes of variability. However, the recent strengthening of the trade winds and the unresolved models biases make these projections of medium confidence (Cai et al., 2015; Timmermann et al., 2018).

Another possible explanation for the diminished DIC' variability is the projected shoaling of the winter mixed layer depth, associated with a reduced heat loss during the cold season. The mixed layer shoaling will cause less mixing of deep rich DIC waters to the surface on both, seasonal and interannual timescales. In the winter deep convection

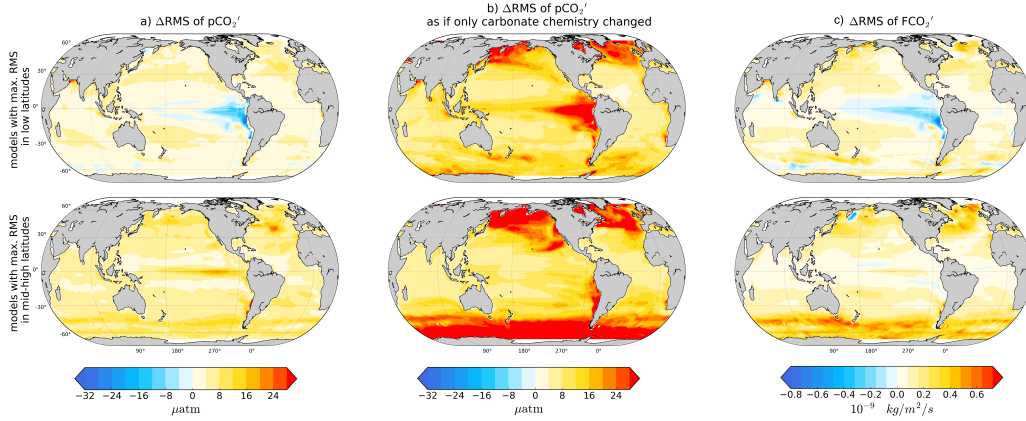


Figure 3. Causes of increasing sea surface $p\text{CO}_2'$ variability: Total change (measured as 2045-2095 minus 1870-1920 values) of **a)** the RMS of $p\text{CO}_2'$, **b)** RMS of $p\text{CO}_2'$ when only the value of $\overline{p\text{CO}_2}$, γ_{DIC_s} and γ_T vary, but we keep constant the 1870-1920 value of the DIC_s' and T' interannual anomalies and **c)** the RMS of FCO_2' . First we compute the total change for each model and subsequently take the ensemble mean of CanESM2, CESM1-BGC and GFDL-ESM2G (**top row**) and HadGEM-CC/ES and MPI-ESM-LR (**bottom row**). Panel **b)** highlights that the RMS of $p\text{CO}_2$ increases due carbonate chemistry changes. However, the interannual variability of DIC and T generates differences between column a) and b) that depend on the models' physical and biological dynamics.

278 regions the future shoaling of the MLD may be underestimated by models, because they
 279 show a shallower than observed present-day mixed layer depth (Downes et al., 2009; Sallée
 280 et al., 2013). Simulations show that a decrease in mixed layer depth will also reduce the
 281 input of macronutrients and therefore reduce primary productivity, this may be reflected
 282 in a reduced DIC variability (Bopp et al., 2013). In other areas, such as the Southern
 283 Ocean, a reduction in the light and temperature limitation prove to increase primary pro-
 284 ductivity (Steinacher et al., 2010) which could counteract the decrease of the DIC vari-
 285 ability in these regions associated with shallower MLD. The total reduction of the DIC
 286 STD may be a combination of these factors; for example, even if ENSO magnitude and
 287 frequency were to increase, a reduction of the MLD may confine the ocean uptake of CO_2
 288 to the surface, thereby reducing the DIC vertical gradient. As a result frequent upwelling
 289 events would have a smaller impact on $p\text{CO}_2$.

290 4 Summary and Conclusions

291 The ocean surface $p\text{CO}_2$ responds to climate modes of variability that alter the ocean's
 292 circulation and biogeochemical conditions on interannual time-scales (Resplandy et al.,
 293 2015). Two opposing mechanisms control future changes in $p\text{CO}_2$ IAVA; a higher back-
 294 ground CO_2 concentration together with an increased sensitivity to DIC that enhances
 295 the $p\text{CO}_2$ response to changes in T and DIC, and a reduction of the DIC' IAV that coun-
 296 teracts the $p\text{CO}_2$ IAVA. In the end, although DIC' changes will be smaller compared to
 297 present-day, the ocean will be much more sensitive to them, resulting in an overall $p\text{CO}_2'$
 298 variability increase in most of the global ocean.

299 The future $p\text{CO}_2$ interannual response to greenhouse gases varies with latitude; most
 300 models show that the high latitudes with large $p\text{CO}_2$ IAV are also the ones that will be
 301 exposed to larger amplification, because the buffering capacity decreases faster in this
 302 region (Eggleston et al., 2010). The mid-latitudes variability will be mildly amplified by

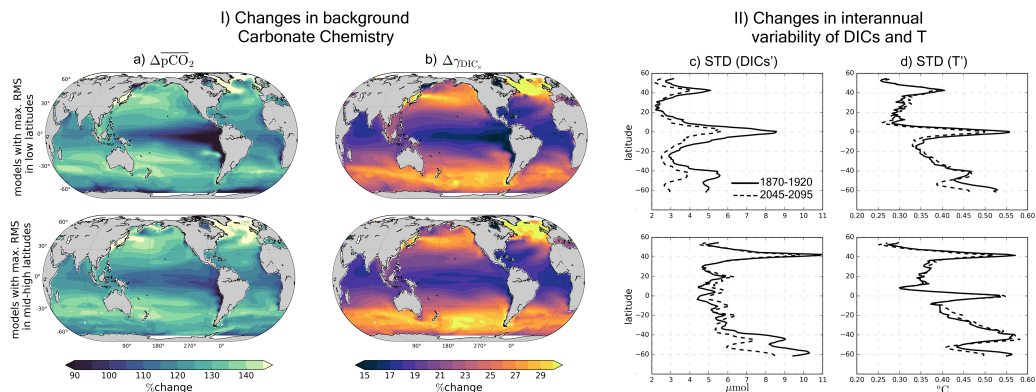


Figure 4. Changes in carbonate chemistry and interannual variability of surface DIC_s' and T' . Percentage change (measured as 2045-2095 minus 1870-1920 values) of **a)** $\overline{pCO_2}$ and **b)** γ_{DIC_s} . A 100% change indicates a doubling in magnitude. **c)** and **d)** show the ensemble mean of the zonally averaged standard deviation of DIC_s' and T' respectively. The **top** row shows the ensemble mean for models CanESM2, CESM1-BGC and GFDL-ESM2G and the **bottom** for HadGEM-CC/ES and MPI-ESM-LR.

303 a larger pool of CO_2 that magnifies the response to T variability. In the equatorial Pa-
 304 cific the models show a larger discrepancy; the models that agree with present-day ob-
 305 servations project a decrease in equatorial pCO_2 IAV due to the reduction of the DIC'
 306 variability that overcompensates the increased DIC sensitivity. On the other hand, the
 307 HadGEM2-CC/ES and MPI-ESM-LR models show a future small increase in this region,
 308 because their pCO_2 IAV is dominated by T instead of DIC.

309 An unresolved issue is how a future increase in CO_2 emissions will affect the CO_2
 310 flux budget. We showed that the FCO_2 anomalies also experience an increase in vari-
 311 ability, that follows the pattern of the pCO_2 IAVA but is modulated by wind speed and
 312 solubility variations not accounted for in the present work. The FCO_2 IAVA disagree with
 313 the result of Dong et al. (2016) who found no increase in FCO_2 IAV on the CMIP5 mod-
 314 els. The reason behind this discrepancy is that Dong et al. (2016) compared the STD
 315 of the FCO_2 anomalies between pre-industrial and present day levels, while we compared
 316 the end of the century levels with those at the onset of the industrial revolution. The
 317 increase in IAV is gradual and remains small at the beginning of the 21st. Therefore, longer
 318 time series are needed to detect the amplification. In another study, Keller et al. (2015)
 319 studied ENSO variability in CESM1-BGC for the 850-2100 period, the authors found
 320 that the warmest period had the lowest variance in ENSO, and that the air-sea CO_2 flux
 321 response was the lowest. The later result agrees with our finding that the pCO_2 vari-
 322 ability decreases in the eastern equatorial Pacific for this model.

323 Changes of surface ocean pCO_2 on interannual time scales not only affect the source/sink
 324 nature of the ocean, but also they may generate in the high latitudes acidification and
 325 hypercapnia episodes on interannual time-scales (McNeil & Sasse, 2016; Sasse et al., 2015).
 326 In the mean time, future projections rely on ocean models as the current datasets are
 327 sparse and lack time continuity. The model's differences and similarities highlight the
 328 large gap in knowledge about the complex physical and biological factors modulated by
 329 ocean-atmosphere interactions that control the interannual variability, but also prove the
 330 undeniable consequences of the changing background carbonate chemistry.

331 **Acknowledgments**

332 This work was supported by the National Science Foundation under Grant No. 1314209.
 333 A.T is supported by the Institute for Basic Science (IBS), South Korea under IBS-R028-
 334 D1. R.E.Z. acknowledges support from the US NSF (OCE15-58699). The CMIP5 data
 335 used in the analysis were obtained from <https://esgf-node.llnl.gov/projects/esgf-llnl/> (last
 336 access: June 2019; Taylor et al. (2012)). The Landschützer et al. (2017) pCO₂ data prod-
 337 uct is available at <https://www.nodc.noaa.gov/archive/arc0105/0160558/3.3/data/0-data/>
 338 (last access: June 2019).

339 **References**

- 340 Bakker, D. C. E., Pfeil, B., Landa, C. S., Metzl, N., O'Brien, K. M., Olsen, A., . . .
 341 et al. (2016). A multi-decade record of high-quality fCO₂ data in version 3 of
 342 the Surface Ocean CO₂ Atlas (SOCAT). *Earth Syst. Sci. Data*, *8*, 383-413.
- 343 Bakker, D. C. E., Pfeil, P., Smith, K., Hankin, S., Olsen, A., & et al. (2014). An
 344 update to the Surface Ocean CO₂ Atlas (SOCAT version 2). *Earth Syst. Sci.*
 345 *Data*, *6*, 69-90.
- 346 Bates, N. R., Astor, Y. M., Church, M. J., Currie, K., Dore, J. E., Gonzalez-Davila,
 347 M., . . . Santana-Casiano, J. M. (2014). A Time-Series View of Changing
 348 Ocean Chemistry Due to Ocean Uptake of Anthropogenic CO₂ and Ocean
 349 Acidification. *Oceanography*, *27*(1), 126-141.
- 350 Bopp, L., Resplandy, L., Orr, J. C., Doney, S. C., Dunne, J. P., Gehlen, M., . . .
 351 Vichi, M. (2013). Multiple stressors of ocean ecosystems in the 21st century:
 352 projections with CMIP5 models. *Biogeosciences*, *10*, 6225–6245.
- 353 Cai, W., Santoso, A., Wang, G., Yeh, S., An, S., Cobb, K. M., & et al. (2015).
 354 ENSO and greenhouse warming. *Nature Climate Change*, *5*, 849-859.
- 355 Cai, W., Wang, G., Dewitte, B., Wu, L., Santoso, A., Takahashi, K., . . . McPhaden,
 356 M. J. (2018). Increased variability of eastern Pacific El Niño under greenhouse
 357 warming. *Nature*, *564*(7735), 201–206. Retrieved from [https://doi.org/](https://doi.org/10.1038/s41586-018-0776-9)
 358 [10.1038/s41586-018-0776-9](https://doi.org/10.1038/s41586-018-0776-9) doi: 10.1038/s41586-018-0776-9
- 359 Chatterjee, A., Gierach, M. M., Sutton, A. J., Feely, R. A., Crisp, D., Elderling, A.,
 360 . . . Schimel, D. S. (2017). Influence of El Niño on atmospheric CO₂ over
 361 the tropical Pacific Ocean: Findings from NASA's OCO-2 mission. *Science*,
 362 *358*(6360).
- 363 Cosca, C. E., Feely, R. A., Boutin, J., Etcheto, J., & McPhaden, M. J. (2003).
 364 Seasonal and interannual CO₂ fluxes for the central and eastern equatorial
 365 Pacific Ocean as determined from fCO₂-SST relationships. *J. Geophys. Res.*,
 366 *108*(C8)(3278).
- 367 Dickson, A. G. (1990). Thermodynamics of the dissociation of boric acid in syn-
 368 thetic seawater from 273.15 to 318.15 K. *Deep-Sea Research Part A. Oceanog-*
 369 *raphic Research Papers*, *37*, 755–766.
- 370 Doney, S. C., Lima, I., Feely, R. A., Glover, D. M., Lindsay, K., Mahowald, N., . . .
 371 Wanninkhof, R. (2009). Mechanisms governing interannual variability in
 372 upper-ocean inorganic carbon system and air-sea CO₂ fluxes: Physical climate
 373 and atmospheric dust. *Deep Sea Research Part II: Topical Studies in Oceanog-*
 374 *raphy*, *56*(8), 640 - 655. doi: <https://doi.org/10.1016/j.dsr2.2008.12.006>
- 375 Dong, F., Li, Y., & Wang, B. (2017). Assessment of responses of tropical Pacific
 376 air-sea CO₂ flux to ENSO in 14 CMIP5 models. *Journal of Climate*, *30*, 8595-
 377 8613.
- 378 Dong, F., Li, Y., Wang, B., Huang, W., Shi, Y., & Dong, W. (2016). Global Air-Sea
 379 CO₂ Flux in 22 CMIP5 Models: Multiyear Mean and Interannual Variability.
 380 *Journal of Climate*, *29*(7), 2407-2431.
- 381 Downes, S. M., Bindoff, N. L., & Rintoul, S. R. (2009). Impact of climate change on
 382 the subduction of mode and intermediate water masses in the Southern Ocean.

- 383 *Journal of Climate*, *22*, 3289-3302.
- 384 Egleston, E. S., Sabine, C. L., & Morel, F. M. M. (2010). Revelle revisited: Buffer
385 factors that quantify the response of ocean chemistry to changes in DIC and
386 alkalinity. *Global Biogeochem. Cycles*, *24*, GB1002.
- 387 Fassbender, A. J., Sabine, C. L., & Palevsky, H. I. (2017). Nonuniform ocean acidifi-
388 cation and attenuation of the ocean carbon sink. *Geophysical Reserach Letters*,
389 *44*, 8404–8413.
- 390 Feely, R. A., Takahashi, T., Wanninkhof, R., McPhaden, M. J., Cosca, C. E.,
391 Sutherland, S. C., & Carr, M. E. (2006). Decadal variability of the air-sea
392 CO₂ fluxes in the equatorial Pacific Ocean. *J. Geophys. Res.*, *111*(C08S90).
- 393 Feely, R. A., Wanninkhof, R., Takahashi, T., & Tans, P. (1999). Influence of El-Niño
394 on the Equatorial Pacific contribution to atmospheric CO₂ accumulation. *Nature*,
395 *398*, 597-601.
- 396 Friedrich, T., Oschlies, A., & Eden, C. (2006). Role of wind stress and heat fluxes in
397 generating interannual-to-decadal variability of air-sea CO₂ and O₂ fluxes in a
398 North Atlantic model. *Geophysical Reserach Letters*, *33*(LS21S04).
- 399 Gallego, M. A., Timmermann, A., Friedrich, T., & Zeebe, R. E. (2018). Drivers of
400 future seasonal cycle changes in oceanic pCO₂. *Biogeosciences*, *15*, 5315-5327.
- 401 Gorgues, T., Aumont, O., & Rodgers, K. B. (2010). A mechanistic account of
402 increasing seasonal variations in the rate of ocean uptake of anthropogenic
403 carbon. *Biogeosciences*, *7*, 2581–2589.
- 404 Hauck, J., & Völker, C. (2015). Rising atmospheric CO₂ leads to large impact of
405 biology on Southern Ocean CO₂ uptake via changes of the Revelle factor. *Geo-*
406 *physical Reserach Letters*, *42*, 1459–1464.
- 407 Hauri, C., Friedrich, T., & Timmermann, A. (2015). Abrupt onset and prolon-
408 gation of aragonite undersaturation events in the Southern Ocean. *Nat. Clim.*
409 *Change*, *6*, 172–176.
- 410 IPCC. (2013). *IPCC Climate Change 2013: The Physical Science Basis. Contri-*
411 *bution of Working Group i to the Fifth Assessment Report of the Intergovern-*
412 *mental Panel on Climate Change*. Cambridge, United Kingdom and New York,
413 NY, USA: Cambridge University Press.
- 414 Jin, C., Zhou, T., & Chen, X. (2019). Can CIMP5 Earth System Models repro-
415 duce the interannual variability of air-sea CO₂ fluxes over the tropical Pacific
416 Ocean? *J. Climate*, *32*, 2261-2275.
- 417 Keller, K. M., Joos, F., Lehner, F., & Raible, C. C. (2015). Detecting changes in
418 marine responses to ENSO from 850 to 2100 C.E.: Insights from the ocean
419 carbon cycle. *Geophysical Reserach Letters*, *42*.
- 420 Landschützer, P., Gruber, N., & Bakker, D. (2017). *An updated observation-based*
421 *global monthly gridded sea surface pCO₂ and air-sea CO₂ flux product from*
422 *1982 through 2015 and its monthly climatology (NCEI Accession 0160558).*
423 *Version 2.2. NOAA National Centers for Environmental Information. Dataset.*
424 *doi:10.7289/v5z899n6.*
- 425 Landschützer, P., Gruber, N., Bakker, D. C. E., Stemmler, I., & Six, K. D. (2018).
426 Strengthening seasonal marine CO₂ variations due to increasing atmospheric
427 CO₂. *Nat. Clim. Change*, *8*, 146–150.
- 428 Landschützer, P., Ilyina, T., & Lovenduski, N. (2019). Detecting regional modes of
429 variability in observation-based surface ocean pCO₂. *Geophysical Reserach Let-*
430 *ters*, *46*, 2670-2679.
- 431 Le Quéré, C., Andrew, R. M., Friedlingstein, P., Sitch, S., Hauck, J., Pongratz, J., et
432 al. (2018). Global carbon budget 2018. *Earth Syst. Sci. Data Discuss*(1-3).
- 433 Le Quéré, C., Orr, J. C., Monfray, P., & Aumont, O. (2000). Interannual variability
434 of the oceanic sink of CO₂ from 1979 through 1997. *Global Biogeochem. Cy-*
435 *cles*, *14*(4), 1247-1265.
- 436 Long, M., Lindsay, K., Peacock, S., Moore, J. K., & Doney, S. C. (2013). Twentieth-
437 century oceanic carbon uptake and storage in CESM1(BGC). *J. Climate*, *26*,

- 6775-6800.
- 438 Lovenduski, N. S., Gruber, N., Doney, S. C., & Lima, I. D. (2007). Enhanced
439 CO₂ outgassing in the Southern Ocean from a positive phase of the Southern
440 Annular Mode. *Global Biogeochem. Cycles*, *21*, GB2026.
- 441 McKinley, G. A., Follows, M. J., & Marshall, J. (2004). Mechanisms of air-sea
442 CO₂ flux variability in the equatorial Pacific and the North Atlantic. *Global
443 Biogeochem. Cycles*, *18*(GB2011).
- 444 McNeil, B. I., & Sasse, T. P. (2016). Future ocean hypercapnia driven by anthro-
445 pogenic amplification of the natural CO₂ cycle. *Nature*, *529*, 383–386.
- 446 Millero, F. J. (1995). Thermodynamics of the carbon dioxide system in the oceans.
447 *Geochemica et Cosmochemica Acta*, *59*, 661–677.
- 448 Millero, F. J., Graham, T. B., Huang, F., Bustos-Serrano, H., & Pierrot, D. (2006).
449 Dissociation constants of carbonic acid in seawater as a function of salinity and
450 temperature. *Marine Chemistry*, *100*(1–2), 80–94.
- 451 Park, G. H., Wanninkhof, R., Doney, S. C., Takahashi, T., Lee, K., Feely, R. A., ...
452 Triñanes, J. (2010). Variability of global net sea–air CO₂ fluxes over the last
453 three decades using empirical relationships. *Tellus B*, *62B*, 352–368.
- 454 Resplandy, L. R., Séférian, R., & Bopp, L. (2015). Natural variability of CO₂: What
455 can we learn from centuries-long climate models simulations? *J. Geophys. Res.
456 Oceans*, *120*, 384–404.
- 457 Rödenbeck, C., Bakker, D., Metzl, N., Olsen, A., Sabine, C., Cassar, N., ...
458 Heimann, M. (2014). Interannual sea–air CO₂ flux variability from an
459 observation-driven ocean mixed-layer scheme. *Biogeosciences*, *11*, 4599–4613.
- 460 Rödenbeck, C., Bakker, D. C. E., Gruber, N., Iida, Y., Jacobson, A. R., Jones, S.,
461 ... Zeng, J. (2015). Data-based estimates of the ocean carbon sink variability
462 – first results of the Surface Ocean pCO₂ Mapping intercomparison (SOCOM).
463 *Biogeosciences*, *12*, 7251–7278.
- 464 Sabine, C. L., Hankin, S., Koyuk, H., Bakker, D. C. E., Pfeil, B., Olsen, A., ... oth-
465 ers (2013). Surface Ocean CO₂ Atlas (SOCAT) gridded data products. *Earth
466 Syst. Sci. Data*, *5*, 145–153.
- 467 Sallée, J. B., Shuckburgh, E., Bruneau, N., Meijers, A. J. S., Bracegirdle, T. J., &
468 Wang, Z. (2013). Assessment of Southern Ocean mixed-layer depths in CMIP5
469 models: Historical bias and forcing response. *Geophysical Research Oceans*,
470 *118*, 1845–1862.
- 471 Sasse, T., McNeil, B. I., Matear, R., & Lenton, A. (2015). Quantifying the influence
472 of CO₂ seasonality on future aragonite undersaturation onset. *Biogeosciences*,
473 *12*, 6017–6031.
- 474 Steinacher, M., Joos, F., Froelicher, T. L., Bopp, L., Cadule, P., Cocco, V., ...
475 Segschneider, J. (2010). Projected 21st century decrease in marine productiv-
476 ity: a multi-model analysis. *Biogeosciences*, *7*, 979–1005.
- 477 Sutton, A. J., Feely, R. A., Sabine, C. L., McPhaden, M. J., Takahashi, T., Chavez,
478 F. P., ... Mathis, J. T. (2014). Natural variability and anthropogenic change
479 in equatorial Pacific surface ocean pCO₂ and pH. *Global Biogeochem. Cycles*,
480 *28*, 131–145.
- 481 Sutton, A. J., Wanninkhof, R., Sabine, C. L., Feely, R. A., Cronin, M. F., & Weller,
482 R. A. (2017). Variability and trends in surface seawater pCO₂ and CO₂ flux in
483 the Pacific Ocean. *Geophysical Research Letters*, *44*, 5627–5636.
- 484 Takahashi, T., Sutherland, S. C., Sweeney, C., Poisson, A., Metzl, N., Tilbrook, B.,
485 ... Nojiri, Y. (2002). Global sea–air CO₂ flux based on climatological sur-
486 face ocean pCO₂, and seasonal biological and temperature effects. *Deep-Sea
487 Research II*, *49*, 1601–1623.
- 488 Taylor, K. E., Stouffer, R. J., & Meehl, G. A. (2012). An Overview of CMIP5 and
489 the experiment design. *B. Am. Meteorol. Soc.*, *93*, 485–489.
- 490 Timmermann, A., An, S., Kug, J., Jin, F., Cai, W., Capotondi, A., ... et al. (2018).
491 El Niño–Southern Oscillation complexity. *Nature*, *559*(7715), 535–543.

- 493 Timmermann, A., Oberhuber, J., Bacher, A., Esch, M., Latif, M., & Roeckner, E.
494 (1999). Increased El Niño frequency in a climate model forced by future green-
495 house warming. *Nature*, *398*(6729), 694-697.
- 496 Tjiputra, J. F., Olsen, A. R. E., Bopp, L., Lenton, A., Pfeil, B., Roy, T., . . . Heinze,
497 C. (2014). Long-term surface pCO₂ trends from observations and models.
498 *Tellus B*, *66*(23083).
- 499 Valsala, V. K., Roxy, M. K., Ashok, K., & Murtugudde, R. (2014). Spatiotempo-
500 ral characteristics of seasonal to multidecadal variability of pCO₂ and air-sea
501 CO₂ fluxes in the equatorial Pacific Ocean. *J. Geophys. Res. Oceans*, *119*,
502 8987–9012.
- 503 Vecchi, G. A., Soden, B. J., Wittenberg, A. T., Held, I. M., & Leetmaa, A. (2006).
504 Weakening of tropical Pacific atmospheric circulation due to anthropogenic
505 forcing. *Nature*, *441*, 73-76.
- 506 Verdy, A., Dutkiewicz, S., Follows, M. J., Marshall, J., & Czaja, A. (2007). Carbon
507 dioxide and oxygen fluxes in the Southern Ocean: Mechanisms of interannual
508 variability. *Global Biogeochem. Cycles*, *21*(GB2020).
- 509 Wang, X., Murtugudde, R., Hackert, E., Wang, J., & Beauchamp, J. (2015). Sea-
510 sonal to decadal variations of sea surface pCO₂ and sea-air CO₂ flux in the
511 equatorial oceans over 1984–2013: A basin-scale comparison of the Pacific and
512 Atlantic Oceans. *Global Biogeochem. Cycles*.
- 513 Zeebe, R. E., & Wolf-Gladrow, D. (2001). *CO₂ in Seawater: Equilibrium, Kinetics,*
514 *Isotopes*. Amsterdam, Netherlands, and Philadelphia, PA, USA: Elsevier Sci-
515 ence.
- 516 Zhao, X., & Allen, R. J. (2019). Strengthening of the Walker Circulation in re-
517 cent decades and the role of natural sea surface temperature variability. *Envi-*
518 *ron. Res. Commun*, *1*(021003).